Electron Microscopy

DOI: 10.1002/anie.201004638

Oxygen-Vacancy Ordering at Surfaces of Lithium Manganese(III,IV) Oxide Spinel Nanoparticles**

*Rong Huang, Yumi H. Ikuhara, Teruyasu Mizoguchi, Scott D. Findlay, Akihide Kuwabara, Craig A. J. Fisher, Hiroki Moriwake, Hideki Oki, Tsukasa Hirayama, and Yuichi Ikuhara**

Cathode materials such as $LiCoO_2$ and $LiMn_2O_4$ are the key components determining the performance of a lithium ion battery.[1] The complicated microstructural changes and phase transitions taking place in these materials during the charge/discharge cycle critically influence battery lifetime. Direct observation of light elements with atomic-level resolution is necessary to elucidate the rich phenomena related to their charge/discharge behavior and capacity fading. Here we report for the first time direct observation of Li and O atoms in nanoparticles of $LiMn_2O_4$ using a spherical aberration (C_s) corrected scanning transmission electron microscope (STEM).[2]

Lithium manganese oxide spinel ($LiMn_2O_4$) is a promising cathode material for lithium ion batteries,[3] and has the cubic spinel structure (space group $Fd\bar{3}m$) with a lattice parameter of $a = 8.2449$ Å at room temperature (Figure 1 a). In stoichiometric $LiMn_2O_4$, half of the manganese exists as Mn^{3+} and the other half as Mn^{4+}, with the ions distributed randomly throughout the crystal at room or higher temperatures. A phase transition has been observed slightly below room temperature from cubic to orthorhombic symmetry.[4] This is attributed to charge ordering of Mn^{3+} and Mn^{4+} ions as a result of cooperative interactions between Jahn–Teller-distorted Mn^{3+} ions on the octahedral site. The presence of oxygen vacancies, which can be introduced by altering the synthesis conditions and starting reagents,[5] leads to a higher proportion of Mn^{3+} relative to Mn^{4+}, which affects the degree of Jahn–Teller-induced ordering. For example, a tetragonal spinel phase (space group $I4_1/amd$) has been observed in $LiMn_2O_{4-\delta}$ above room temperature by neutron powder diffraction.[6] In contrast to the relatively heavy manganese ions, the detailed local structures of Li and O are still not well elucidated because of the difficulty of detecting and characterizing light elements. Such information is critical to understanding the electrochemical processes occurring during battery use.

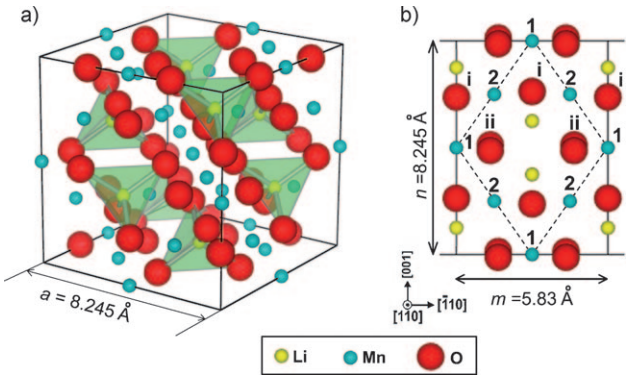

Figure 1. . The $LiMn_2O_4$ spinel structure. a) Unit cell (space group $Fd\bar{3}m$). b) Projection along the [110] zone axis showing separate Li, O, and Mn columns. Mn-1 and Mn-2 columns have different atom densities, and O-ii columns are slightly misaligned.

An STEM equipped with an annular dark-field (ADF) detector and electron energy-loss spectrometer (EELS) can provide useful structural and chemical information with atomic resolution. It also has the advantage that image contrast is roughly proportional to the square of the atomic number Z.[7] Adding a spherical-aberration corrector (C_s corrector) to the STEM dramatically improves the spatial resolution, and makes it possible to discern sub-Ångström detail. A wide spectrum of defective structures in various materials have been observed by using C_s-corrected STEMs.[8] Recently, annular bright-field (ABF) STEM imaging has been successfully used to image columns of both light and heavy elements simultaneously with good signal-to-noise ratio.[9] This is a very promising technique because of its sensitivity to light elements and the robust interpretation of direct images for a large range of sample thicknesses.[9]

Attempts have been made to visualize Li sites in cathode materials to better understand the structures and conduction mechanisms in lithium ion batteries, but so far with limited success. For example, STEM observation of Li extraction/insertion in $Li_{1.2}Mn_{0.4}Fe_{0.4}O_2$ has been reported, but only at low magnification based on EELS mapping.[10] By using a C_s-

[*] Dr. R. Huang
Nanostructures Research Laboratory, Japan Fine Ceramics Center
Nagoya 456-8587 (Japan)
and
Key Laboratory of Polar Materials and Devices, Ministry of Education, East China Normal University, Shanghai 200062 (P. R. China)
Dr. Y. H. Ikuhara, Dr. A. Kuwabara, Dr. C. A. J. Fisher, Dr. H. Moriwake, Dr. T. Hirayama, Prof. Y. Ikuhara
Nanostructures Research Laboratory, Japan Fine Ceramics Center
Nagoya 456-8587 (Japan)
Fax: (+81) 3-5841-7694
E-mail: ikuhara@sigma.t.u-tokyo.ac.jp
Dr. T. Mizoguchi, Dr. S. D. Findlay, Prof. Y. Ikuhara
Institute of Engineering Innovation, The University of Tokyo, Tokyo 113-8656 (Japan)
Dr. H. Oki
Toyota Motor Corporation, Shizuoka, 410-1193 (Japan)

[**] Part of this research was supported by the Japan Society for the Promotion of Science (JSPS) through its Funding Program for World-Leading Innovative R&D on Science and Technology (FIRST Program).

corrected STEM, Li sites in olivine-structured $LiFePO_4$ have also been visualized on the atomic scale with an ADF detector. However, only indirect evidence based on the presence of antisite Fe ions (i.e., Fe ions on Li sites) could be provided.[11]

Previously, Li ions in $LiCoO_2$ could be visualized by using a high-resolution transmission electron microscope (HRTEM).[12] However, this required focal-series reconstruction of the specimen exit surface wave from twenty different images, and thus does not constitute direct visualization of Li in real time. A combination of ADF and ABF techniques in a C_s-corrected STEM, in contrast, allows direct observation of Li and O ions without further image processing, and thus is a less time consuming method for reliably identifying positions of light elements.

The [110] projection of $LiMn_2O_4$ is most suitable for observing Li, O, and Mn ions directly, because separate columns of these ions are aligned in this direction (Figure 1b). Eight Mn columns form a diamond configuration, with two Li columns separated by 2.06 Å at the center. In the cubic structure, the ratio of the projected distance along the short diagonal to the distance along the long diagonal is 0.707. Furthermore, the O atoms in the O-ii columns are slightly misaligned along the [110] direction (Figure 1b), and the number of Mn atoms in the Mn-1 column is twice that of the Mn-2 columns.

Tetragonal (oxygen-deficient) lithium manganese spinel has lattice constants $a = b = 5.7356$ Å and $c = 8.6464$ Å,[6b] which correspond to pseudo-cubic lattice parameters $a_c = b_c = 8.1114$ Å and $c_c = 8.6464$ Å. The diamonds demarcated by Mn columns along the $\langle 110\rangle_{cubic}$ zone axis group are no longer isotropic because of the tetragonal distortion, and degenerate into $[100]_{tetragonal}$, $[010]_{tetragonal}$, and $[111]_{tetragonal}$ zone axes. The Mn diamonds along $[100]_{tetragonal}$ and $[010]_{tetragonal}$ are equivalent, but different from that of the $[111]_{tetragonal}$ projection. The short and long diagonals of the Mn diamond viewed along $[100]_{tetragonal}$ and $[010]_{tetragonal}$ are $m = 5.7356$ Å and $n = 8.6464$ Å, respectively, giving an m/n ratio of 0.663. In contrast, the short and long diagonals of the Mn diamond viewed down the $[111]_{tetragonal}$ zone axis are $m = 5.9278$ Å and $n = 8.1114$ Å, respectively, giving an m/n ratio of 0.731. Thus, measurement of the m/n ratio can be used to distinguish between the tetragonal phase and cubic phase in lithium manganese spinel.

$LiMn_2O_4$ powder was synthesized by pyrolysis in O_2 at 700 °C of a precursor powder prepared by ligand exchange of lithium isopropoxide and manganese ethoxide with 2-ethoxyethanol. The powder consisted of regularly shaped faceted particles roughly 30–120 nm in diameter (Figure 2a).[13] The crystal structure was confirmed to be cubic spinel by X-ray diffraction. Because this material is susceptible to electron-beam damage, all experiments were necessarily carried out in a very short time to obtain reproducible results. Measurements were taken for a large number of particles from four different samples prepared from two different $LiMn_2O_4$ powder batches.

Figure 2b shows a high-angle annular dark-field (HAADF) STEM image of the (111) facet of a typical $LiMn_2O_4$ particle. An EELS line scan was performed from the

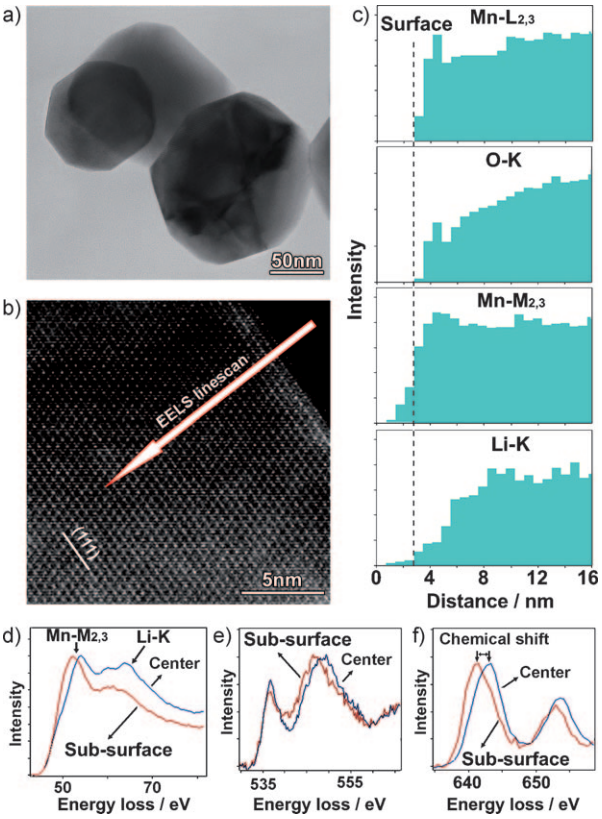

Figure 2. a) TEM image of $LiMn_2O_4$ particles. b) STEM image of the edge of a typical $LiMn_2O_4$ particle. The arrow indicates the region of the EELS line scan. c) Integrated intensity of the Mn-$L_{2,3}$, O-K, Mn-$M_{2,3}$ and Li-K edges. d) ELNES of Mn-$M_{2,3}$ and Li-K showing the difference in Li concentration between the center and surface regions, as well as the chemical shift of Mn-$M_{2,3}$. e) ELNES of O-K edge showing the differences in pre-peak height and main peak position between the center and surface regions. f) ELNES of the Mn-$L_{2,3}$ edge showing a chemical shift from the center to the surface region.

surface to the center of this particle, as indicated by the arrow in Figure 2b. Figure 2c shows the intensity profiles of Mn-$L_{2,3}$, O-K, Mn-$M_{2,3}$, and Li-K signals. The surface is demarcated by a dashed line. A very thin Mn-rich layer is apparent from the Mn-$L_{2,3}$ and M-$M_{2,3}$ profiles. Its width is broadened due to delocalization of the Mn-$M_{2,3}$ edge relative to the Mn-$L_{2,3}$ edge.[14] Other than this Mn-rich surface layer, the distribution of Mn is relatively uniform inside the particle. In contrast, the gradients of the O-K and Li-K intensities increase from the surface to the center region (apart from a small O-rich peak at the surface, which corresponds to the Mn-rich layer).

To obtain more detailed information, we carried out EELS analysis for the center and surface regions of the $LiMn_2O_4$ particle. Figure 2d shows the Mn-$M_{2,3}$ and Li-K energy-loss near-edge fine structure (ELNES) for center and near-surface regions after background subtraction, normalized to the intensity of the Mn-$M_{2,3}$ edge. A higher Li concentration in the center region than the surface region is apparent. In Figure 2e, the O-K edges also show clear differences between the bulk and near-surface regions. The first peak of the O-K edge is less intense in the surface region than in the bulk region. In transition metal (TM) containing

oxides this peak originates from the hybridization between the O 2p and unoccupied TM 3d orbitals;[15] the decrease in magnitude of the first peak corresponds to greater filling of the Mn 3d orbital, which indicates less oxygen in the coordination shell of Mn.[15] The second peak of the O-K edge around 548 eV also changes. Such subtle differences in O-K ELNES peaks are known to be related to changes in the arrangement of anions around the central Mn atoms.[15] In the case of our $LiMn_2O_4$ nanoparticles, this is best explained by the presence of O vacancies.

In Figure 2 f, the Mn-$L_{2,3}$ peak for the subsurface region is seen to shift to about 1.8 eV below that for the center region, which is consistent with the observed chemical shift of Mn-$M_{2,3}$ in Figure 2 d. This indicates that the valence of Mn in the subsurface region is lower than in the center region, which is consistent with the O gradient from the EELS line scan (Figure 2 c). Quantitative analysis of the EELS spectra reveals that the Mn/O ratios increase from 0.50 ± 0.07 in the center region to 0.68 ± 0.09 in the surface region. A tetragonal lithium manganese spinel structure can thus be inferred to exist in the surface region with O and Li deficiency. A recent report suggests this deficiency is an intrinsic feature of nanocrystalline $LiMn_2O_4$,[16] not a result of electron-beam irradiation. This elucidation of the local chemistry of $Li_{1-x}Mn_2O_{4-\delta}$ particles aids interpretation of our ADF images.

Figure 3 a shows a HAADF-STEM image of the subsurface region of a small $LiMn_2O_4$ particle along the $[110]_{cubic}$ zone axis, obtained at a detection angle of $\beta = 92$–228 mrad. The Mn diamond arrangement is clearly seen, with brighter contrast corresponding to the Mn-1 columns and lesser contrast to the Mn-2 columns. No contrast from O or Li sites can be discerned. The ratio of the short and long diagonals of the Mn diamond, measured from the raw HAADF-STEM image, is $m/n = 0.667$. This indicates that the crystal has the tetragonal structure, consistent with the measured oxygen deficiency and expected Jahn–Teller distortion from the EELS analysis. Hereafter, we use the tetragonal indices when referring to these $LiMn_2O_4$ particles.

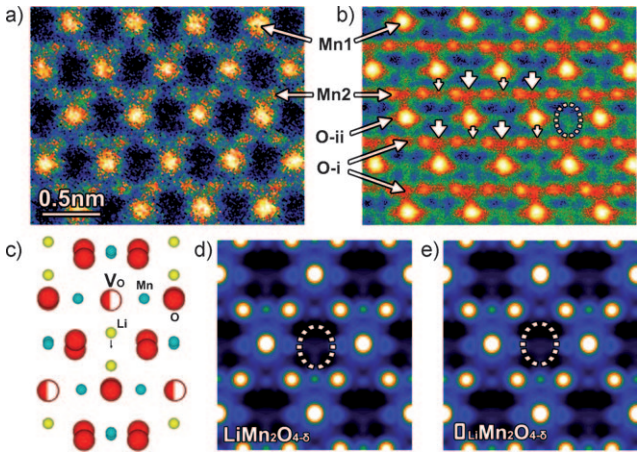

Figure 3. ADF images of a tetragonal $Li_{1-x}Mn_2O_{4-\delta}$ particle along the $[100]_{tetragonal}$ zone axis. a) Detection angle of 92–228 mrad showing the diamond configuration of Mn columns. The Mn-1 and Mn-2 sites have different contrasts. b) Detection angle of 52–140 mrad revealing alternating oxygen contrast levels (large and small arrows) and the shift in O-i columns. Contrast at the center of the Mn diamond is also discernable, indicated by a dashed circle. c) Crystal structure obtained by ab initio calculations showing the shift of Li columns away from the low-density (high-vacancy) O-i columns, viewed along the [100] zone axis. d) Image simulated by using the structure in (c), reproducing the experimental ADF image in (b). e) Simulated image based on the structure in (c) but with Li ions removed, which also shows weak contrast at the center of the Mn diamond. A specimen thickness of 200 Å was assumed for the simulations.

Because Li and O scatter the electron beam only weakly, the spatial distribution of electrons scattered by columns of these ions is confined to a much smaller angle range about the beam direction compared with Mn columns.[17] By using smaller detection angles, it should thus be possible to obtain higher contrast for the Li and O columns. Figure 3 b shows an ADF-STEM image of the subsurface region of an $Li_{1-x}Mn_2O_{4-\delta}$ particle along a $[100]_{tetragonal}$ zone axis obtained with a detection angle of $\beta = 52$–140 mrad. The diamond arrangement of bright Mn-1 columns and darker Mn-2 columns, similar to the HAADF-STEM image in Figure 3 a, is clearly visible. The O columns also have sufficient contrast to be discernable. Interestingly, we find that the intensity of O-i columns is not uniform. They exhibit alternately brighter and darker contrast, as highlighted by the large and small arrows in Figure 3 b. This indicates the presence of vacancies in the dark O-i columns, consistent with the lack of O in the surface region detected by EELS (Figure 2). Furthermore, the bright O-i columns are shifted away from their original sites (midway between two Mn-2 sites), as seen in Figure 3 b. This may be caused by strong Jahn–Teller distortion or the presence of some other defects near the O-i column, for example, a vacancy–interstitial oxygen cluster.[6b] In addition, O-ii columns show weaker contrast than the brighter O-i columns due to the delocalization caused by misalignment of oxygen atoms; these appear as shoulders of Mn-1 site signals because the strong Mn-1 contrast dominates over the weaker contrast of oxygen. Furthermore, very weak contrast near the center of the Mn diamond is discernable, as indicated by a dashed circle in Figure 3 b. This cannot be interpreted intuitively, and will be discussed in more detail below.

To confirm the presence of O vacancies and obtain more information about the location of Li ions, first-principles calculations with the Vienna Ab Initio Simulation Package (VASP)[18] were carried out on the tetragonal $LiMn_2O_{4-\delta}$ structure, assuming 50 % vacancies in alternate O-i columns. The crystal structure after geometry optimization shows that the Li ions are displaced from their ideal positions due to the presence of oxygen vacancies. They move toward the high-density O-i columns and away from the low-density (high-vacancy) O-i columns due to electrostatic repulsion when projected along the [100] zone axis (Figure 3 c).

Based on this structure, we carried out ADF image simulation assuming the same conditions as in the experiment. The simulated image (Figure 3 d) unambiguously reproduces the contrast at oxygen columns (Figure 3 b). Figure 3 d does not reproduce the measured contrast exactly, however, because the oxygen-vacancy concentration in the nanoparticles varies and is thus unlikely to be 50 % at the point where the ADF image was taken. Nevertheless, the good agreement confirms that the ADF images are consistent

with an oxygen-deficient tetragonal phase in the surface region of the $LiMn_2O_{4-\delta}$ particles. As oxygen deficiency in $LiMn_2O_4$ has previously been observed to be a function of the synthesis route and number of charge/discharge cycles,[5,6a] it is unlikely that our identification of ordered vacancies in the surface region of $LiMn_2O_4$ particles is an artifact of the rarefied conditions in the TEM, but rather indicative of a more general phenomenon common to Li–Mn–O-based cathode materials.

The simulated image also reproduces the weak contrast near the center of the Mn diamond (dashed circle in Figure 3d). To verify whether this contrast originates from Li ions or not, we performed an ADF image simulation using the same conditions but with Li ions removed from the crystal structure. The result given in Figure 3e shows essentially the same weak contrast near the center of the Mn diamond (dashed circle in Figure 3e). There are no significant differences between the simulated ADF images of the structures of $LiMn_2O_{4-\delta}$ and $\square_{Li}Mn_2O_{4-\delta}$ (where $\square$ represents vacant sites), that is, this contrast is not a consequence of the presence of Li ions. Thus, unlike the ordering of oxygen vacancies, Li ions cannot be observed directly by ADF under these experimental conditions.

To observe Li ions, ABF imaging was used. Figure 4a shows an ABF image of the subsurface region of an $LiMn_2O_{4-\delta}$ particle viewed along [100] with a detection

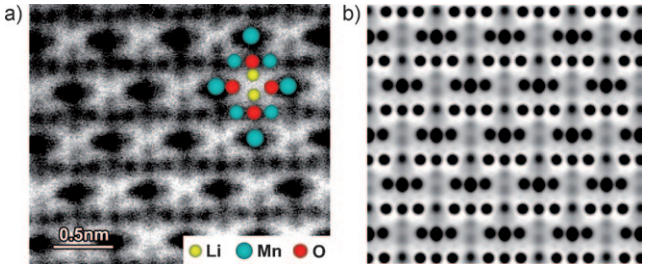

Figure 4. ABF images of tetragonal $LiMn_2O_{4-\delta}$ spinel nanoparticles along zone axis [100]. a) Experimental image for a detection angle of 6–25 mrad. b) Simulated image reproducing the contrast of the experimental image and confirming visualization of Li ions. A specimen thickness of 100 Å was assumed for the simulation.

angle of 6–25 mrad. The Li ions are clearly visible together with the O and Mn columns in the ABF image, as indicated by the model structure overlaid in Figure 4a. They slightly shift away from their original positions due to the presence of O vacancies. However, ABF imaging is less sensitive to the degree of O occupancy compared with ADF imaging, and so the presence of O vacancies is not easily discerned.

Figure 4b shows the corresponding image simulations, again based on the crystal structure obtained from first-principles calculations. This image unambiguously reproduces the image contrast in the experimental ABF image. The good agreement between the experimental and simulated images confirms that the Li ions have been imaged successfully by the ABF technique with a C_s-corrected STEM.

In summary, Li and O deficiencies in $LiMn_2O_4$ spinel nanoparticles have been revealed by EELS analysis with a C_s-corrected STEM. An ordered tetragonal $Li_{1-x}Mn_2O_{4-\delta}$ phase was detected, and the structure subsequently confirmed by first-principles calculations and image simulations. Li ions were visualized directly, situated at the center of Mn diamond configurations. The structural and compositional changes revealed between bulk and surface regions of the nanoparticles undoubtedly influence charge/discharge behavior and capacity fade in lithium ion batteries that use $LiMn_2O_4$ as the cathode material. The results demonstrate that a combination of ADF and ABF techniques permits characterization of defects in crystalline solids with atomic resolution for elements heavier than He.

Experimental Section

STEM observations were performed with a 200 kV JEM-2100F (JEOL) microscope equipped with a spherical-aberration corrector (CEOS GmbH) and a Gatan Image Filter (GIF) for EELS analysis, which provided a minimum probe of about 1 Å in diameter. During *Z*-contrast imaging, a probe convergence angle of 25 mrad and an annular dark-field detector with an inner angle greater than 52 mrad were used. A collection semi-angle of 35 mrad was used in EELS analyses.

First-principles total-energy calculations were carried out using the VASP code based on the projector augmented wave method.[18] The cutoff energy for plane-wave basis sets was 500 eV. The initial structure model was a $2\sqrt{2}\times2\sqrt{2}\times1$ supercell of a tetragonal spinel-like $LiMn_2O_4$ unit cell. A $3\times3\times3$ *k*-mesh was used for irreducible Brillouin zone sampling to ensure that the total energies converged to within 1 meV per formula unit. The effect of strong correlation between Mn 3d electrons was taken into account by using the GGA + *U* method.[19] The value of *U* for the Mn 3d orbital was set at 5 eV.[20] Geometry optimization was performed until residual forces were less than 0.02 eV Å^{-1}.

The STEM image simulations were carried out with the multislice method and the model structure shown in Figure 3c. The experimentally measured values of lens and detector apertures were used in the simulations. Note that the specimen thicknesses assumed may not correspond to those in the experiment.

Received: July 28, 2010
Revised: January 5, 2011
Published online: February 23, 2011

Keywords: electron microscopy · lithium · nanoparticles · solid-state structures · spinel phases

[1] a) J. M. Tarascon, M. Armand, *Nature* **2001**, *414*, 359–367; b) M. S. Whittingham, *Chem. Rev.* **2004**, *104*, 4271–4301.
[2] a) P. E. Batson, N. Dellby, O. L. Krivanek, *Nature* **2002**, *418*, 617–620; b) P. M. Voyles, D. A. Muller, J. L. Grazul, P. H. Citrin, H. J. L. Gossmann, *Nature* **2002**, *416*, 826–829; c) U. Kaiser, D. A. Muller, J. L. Grazul, A. Chavilin, M. Kawasaki, *Nat. Mater.* **2002**, *1*, 102–105; d) P. D. Nellist, M. F. Chisholm, N. Dellby, O. L. Krivanek, M. F. Murfitt, Z. S. Szilagyi, A. R. Lupini, A. Borisevich, W. H. Sides, Jr., S. J. Pennycook, *Science* **2004**, *305*, 1741.
[3] M. M. Thackeray, W. I. F. David, P. G. Bruce, J. B. Goodenough, *Mater. Res. Bull.* **1983**, *18*, 461–472.
[4] a) A. Yamada, M. Tanaka, *Mater. Res. Bull.* **1995**, *30*, 715–721; b) J. Rodríguez-Carvajal, G. Rousse, C. Masquelier, M. Hervieu, *Phys. Rev. Lett.* **1998**, *81*, 4660–4663.

[5] M. Yonemura, A. Yamada, H. Kobayashi, M. Tabuchi, T. Kamiyama, Y. Kawamoto, R. Kanno, *J. Mater. Chem.* **2004**, *14*, 1948 – 1958.
[6] a) P. Strobel, F. L. Cras, L. Seguin, M. Anne, J. M. Tarascon, *J. Solid State Chem.* **1998**, *135*, 132 – 139; b) R. Kanno, A. Kondo, M. Yonemura, R. Gover, Y. Kawamoto, M. Tabuchi, T. Kamiyama, F. Izumi, C. Masquelier, G. Rousse, *J. Power Sources* **1999**, *81–82*, 542 – 546; c) J. Sugiyama, T. Atsumi, T. Hioki, S. Noda, N. Kamegashira, *J. Power Sources* **1997**, *68*, 641 – 645.
[7] a) S. J. Pennycook, D. E. Jesson, *Ultramicroscopy* **1991**, *37*, 14 – 38; b) P. D. Nellist, S. J. Pennycook, *Phys. Rev. Lett.* **1998**, *81*, 4156 – 4159.
[8] a) D. A. Muller, N. Nakagawa, A. Ohtomo, J. L. Grazul, H. Y. Hwang, *Nature* **2004**, *430*, 657 – 661; b) S. Wang, A. Y. Borisevich, S. N. Rashkeev, M. V. Glazoff, K. Sohlberg, S. J. Pennycook, S. T. Pantelides, *Nat. Mater.* **2004**, *3*, 143 – 146; c) J. P. Buban, K. Matsunaga, J. Chen, N. Shibata, W. Y. Ching, T. Yamamoto, Y. Ikuhara, *Science* **2006**, *311*, 212 – 215; d) Y. Sato, J. P. Buban, T. Mizoguchi, N. Shibata, M. Yodogawa, T. Yamamoto, Y. Ikuhara, *Phys. Rev. Lett.* **2006**, *97*, 106802; e) N. Shibata, M. F. Chisholm, A. Nakamura, S. J. Pennycook, T. Yamamoto, Y. Ikuhara, *Science* **2007**, *316*, 82 – 85; f) R. Huang , T. Mizoguchi, K. Sugiura, H. Ohta, K. Koumoto, T. Hirayama, Y. Ikuhara, *Appl. Phys. Lett.* **2008**, *93*, 181907; g) N. Shibata, A. Goto, S.-Y. Choi, T. Mizoguchi, S. D. Findlay, T. Yamamoto, Y. Ikuhara, *Science* **2008**, *322*, 570 – 573; h) O. L. Krivanek, M. F. Chisholm, V. Nicolosi, T. J. Pennycook, G. J. Corbin, N. Dellby, M. F. Murfitt, C. S. Own, Z. S. Szilagyi, M. P. Oxley, S. T. Pantelides, S. J. Pennycook, *Nature* **2010**, *464*, 571 – 574.
[9] S. D. Findlay, N. Shibata, H. Sawada, E. Okunishi, Y. Kondo, T. Yamamoto, Y. Ikuhara, *Appl. Phys. Lett.* **2009**, *95*, 191913.
[10] a) J. Kikkawa, T. Akita, M. Tabuchi, M. Shikano, K. Tatsumi, M. Kohyama, *Electrochem. Solid-State Lett.* **2008**, *11*, A183 – A186; b) J. Kikkawa, T. Akita, M. Tabuchi, M. Shikano, K. Tatsumi, M. Kohyama, *Appl. Phys. Lett.* **2007**, *91*, 054103.
[11] a) S. Y. Chung, S. Y. Choi, T. Yamamoto, Y. Ikuhara, *Phys. Rev. Lett.* **2008**, *100*, 125502; b) S. Y. Chung, S. Y. Choi, T. Yamamoto, Y. Ikuhara, *Angew. Chem.* **2009**, *121*, 551 – 554; *Angew. Chem. Int. Ed.* **2009**, *48*, 543 – 546.
[12] Y. Shao-Horn, L. Croguennec, C. Delmas, E. C. Nelson, M. A. O'Keefe, *Nat. Mater.* **2003**, *2*, 464 – 467.
[13] Y. H. Ikuhara, Y. Iwamoto, K. Kikuta, S. Hirano, *J. Mater. Res.* **1999**, *14*, 3102 – 3110.
[14] K. Kimoto, T. Asaka, T. Nagai, M. Saito, Y. Matsui, K. Ishizuka, *Nature* **2007**, *450*, 702 – 704.
[15] a) H. Kurata, E. Lefèvre, C. Colliex, R. Brydson, *Phys. Rev. B* **1993**, *47*, 13763 – 13768; b) H. Kurata, C. Colliex, *Phys. Rev. B* **1993**, *48*, 2102 – 2108; c) Y. Koyama, T. Mizoguchi, H. Ikeno, I. Tanaka, *J. Phys. Chem. B* **2005**, *109*, 10749 – 10755; d) M. Yoshiya, I. Tanaka, K. Kaneko, H. Adachi, *J. Phys. Condens. Matter* **1999**, *11*, 3217 – 3228.
[16] M. Okubo, Y. Mizuno, H. Yamada, J. Kim, E. Hosono, H. Zhou, T. Kudo, I. Honma, *ACS Nano* **2010**, *4*, 741 – 752.
[17] R. F. Egerton in *Electron energy-loss spectroscopy in the electron microscope*, 2nd ed., Plenum Press, New York, **1996**, p. 136.
[18] a) G. Kresse, J. Furthmüller, *Phys. Rev. B* **1996**, *54*, 11169 – 11186; b) P. E. Blöchl, *Phys. Rev. B* **1994**, *50*, 17953 – 17979.
[19] a) J. P. Perdew, K. Burke, M. Ernzerhof, *Phys. Rev. Lett.* **1996**, *77*, 3865 – 3868; b) S. L. Dudarev, G. A. Botton, S. Y. Savrasov, C. J. Humphreys, A. P. Sutton, *Phys. Rev. B* **1998**, *57*, 1505 – 1509.
[20] F. Zhou, M. Cococcioni, C. A. Marianetti, D. Morgan, G. Ceder, *Phys. Rev. B* **2004**, *70*, 235121.

